PROCEEDINGS OF SPIE

UV, X-Ray, and Gamma-Ray Space Instrumentation for Astronomy XVII

Oswald H. Siegmund
Editor

21–24 August 2011
San Diego, California, United States

Sponsored and Published by
SPIE

Volume 8145

Contents

SESSION 1   X-RAY FOCAL PLANE INSTRUMENTATION

SESSION 4   **SPACE MISSIONS AND INSTRUMENTS II**

POSTER SESSION

Conference Committee

Program Track Chair

Oswald H. Siegmund, University of California, Berkeley (United States)

Conference Chair

Oswald H. Siegmund, University of California, Berkeley (United States)

Program Committee

Matthew N. Beasley, University of Colorado at Boulder (United States)
Michael P. Kowalski, U.S. Naval Research Laboratory (United States)
Stephan R. McCandliss, The Johns Hopkins University (United States)
John V. Vallerga, University of California, Berkeley (United States)
Barry Y. Welsh, University of California, Berkeley (United States)

Session Chairs

1   X-Ray Focal Plane Instrumentation
     Oswald H. Siegmund, University of California, Berkeley (United States)

2   High Energy - Balloon Instrumentation
     Oswald H. Siegmund, University of California, Berkeley (United States)

3   Space Missions and Instruments I
     Erik Wilkinson, Southwest Research Institute (United States)

4   Space Missions and Instruments II
     Jason B. McPhate, University of California, Berkeley (United States)

5   UV - Optical Instrumentation
     Stephan R. McCandliss, The Johns Hopkins University (United States)

6   CCD/CMOS Detectors
     Matthew Beasley, University of Colorado at Boulder (United States)

The Little Photometer That Could: Technical Challenges and Science Results from the *Kepler Mission*

Jon M. Jenkins[∘a], Jeb Dunnuck[b],

[a] SETI Institute/NASA Ames Research Center, M/S 244-30, Moffett Field, CA USA 94305
[b] Ball Aerospace & Technologies Corporation, P.O. Box 1062, Boulder, CO, USA 80306

ABSTRACT

The *Kepler* spacecraft launched on March 7, 2009, initiating NASA's first search for Earth-size planets orbiting Sun-like stars. Since launch, *Kepler* has announced the discovery of 17 exoplanets, including a system of six transiting a Sun-like star, Kepler-11, and the first confirmed rocky planet, Kepler-10b, with a radius of 1.4 that of Earth. *Kepler* is proving to be a cornucopia of discoveries: it has identified over 1200 candidate planets based on the first 120 days of observations, including 54 that are in or near the habitable zone of their stars, and 68 that are 1.2 Earth radii or smaller. An astounding 408 of these planetary candidates are found in 170 multiple systems, demonstrating the compactness and flatness of planetary systems composed of small planets. Never before has there been a photometer capable of reaching a precision near 20 ppm in 6.5 hours and capable of conducting nearly continuous and uninterrupted observations for months to years. In addition to exoplanets, *Kepler* is providing a wealth of astrophysics, and is revolutionizing the field of asteroseismology. Designing and building the *Kepler* photometer and the software systems that process and analyze the resulting data to make the discoveries presented a daunting set of challenges, including how to manage the large data volume. The challenges continue into flight operations, as the photometer is sensitive to its thermal environment, complicating the task of detecting 84 ppm drops in brightness corresponding to Earth-size planets transiting Sun-like stars.

Keywords: *Kepler Mission*, exoplanet, transit, photometry, data compression, systematic error correction

1. INTRODUCTION

The *Kepler* spacecraft was launched in March 2009 as NASA's first mission capable of finding Earth-size planets orbiting Sun-like stars. This mission has been a spectacular success in terms of revolutionizing both the fields of extrasolar planets and of asteroseismology, the study of stellar oscillations. Over 1200 planetary candidates were detected in the first 120 days of observations,[1] effectively tripling the number of known extrasolar planets as of February 2011. Most of these candidates are as small or smaller than Neptune. *Kepler* finds multiple planet candidates transiting a star ∼17% of the time. With the capability to conduct observations for at least 10 years and a photometric precision approaching 20 ppm on 6.5-hr timescales, *Kepler* is poised to reach its primary goal of determining the frequency and distribution of rocky planets in the habitable zone (HZ) of solar-like stars, that range of distances for which liquid water could pool on the surface of a terrestrial planet. However, the success of the *Kepler Mission* wasn't always a foregone conclusion.

This paper describes some of the major challenges facing *Kepler* both before and after launch. These challenges have been mitigated by a combination of good design, great hardware, flexible software and the talented people involved in the mission. It required collaboration between the engineers and scientists who designed and built the photometer and spacecraft and those who process and analyze the exquisite photometric data. We focus on some of the key challenges that were met handily by the design, including the performance of the onboard compression scheme and the approach to target management, and some issues that have arisen after launch when we had the first opportunity to see how a photometer such as *Kepler* would perform in the space environment. It's true that these one-of-a-kind machines never cease to amaze or surprise us when they are finally in orbit and operating, in part, because we cannot truly replicate the totality of the space environment in the laboratory. Also, we cannot ever anticipate the myriad complexity of nature when we observe it with a new and much more powerful instrument than has been previously available. We give examples of how we are dealing with some of the post-launch complexities in ground-processing software, including the thermal sensitivity of the photometer. We provide an update on the key scientific achievements obtained with *Kepler* to date. Finally, we conclude with some thoughts on what the future holds for *Kepler*, and how our experience with this marvelous machine can provide lessons for future space missions, such as ESA's envisioned PLATO space transit survey.

[∘]Send correspondence to J.M.J.: E-mail: Jon.Jenkins@nasa.gov

xi

2. KEY CHALLENGES

In 1994, the first proposal for *Kepler* to NASA's Discovery Program was turned down as too expensive and too risky from a technical perspective. In fact, *Kepler* was rejected by the next two Discovery panels in 1996 and 1998, but was ultimately selected for launch in the fourth Discovery Program competition in 2001 after several years of dedicated and intense efforts to demonstrate the technical and budgetary feasibility of the mission in the face of many significant technical challenges.

Kepler's goal is simple: to observe a large sample of solar-like stars (those burning hydrogen in their cores) to detect periodic dimming in brightness caused when a small planet transits, i.e., crosses the face of its star as it swings around in its orbit, as viewed by the spacecraft. There are several complications with this approach:

First, the dimming caused by a small planet transiting its star is very slight. Planets are rather small compared to the size of stars, even main-sequence stars, *e.g.*, our Sun, which are called dwarfs in comparison to their older, evolved brothers, the giant stars, which burn helium in their cores. The amplitude of the dimming during transit is the ratio of the area blocked by the planet to the total area of the star. Jupiter is about 10% the radius of the Sun, so its transits block 1% of the light as viewed by an extrasolar observer. By comparison, Earth is about 10% the radius of Jupiter and consequently causes a 0.01% or 1 part in 10,000 drop in brightness when it transits the Sun. Since the opportunity to detect a signal arises only when the signal is strong compared to the observational noise, robustly detecting an Earth-size planet transiting a Sun-like star requires a signal-to-noise ratio (SNR) of at least $4\,\sigma$ over the duration of a typical transit, $\sim$6.5 hours in order to build up a total SNR $> 8\,\sigma$ from four or more transit events. The threshold of $7.1\,\sigma$ is required in light of the large number ($\sim 10^{12}$) of statistical tests performed to identify the transit sequences, since we don't know the period or the time of first transit.[2,3] In the 1990s, the precision achieved by state of the art differential photometry from the ground with Charge Coupled Devices (CCDs) was $\sim$0.1%, and could not be achieved easily on a routine basis even with 4-m class telescopes due to atmospheric effects such as extinction, and scintillation,[4] which continue to limit the precision of ground-based photometry.

The *Kepler* concept called for balancing the three major sources of noise to achieve a single transit SNR of 4σ for an 84-ppm, 6.5-hr transit of a G2V star by an Earth-size planet in a one-year orbit. This point design established the three major noise sources and their required values as: 1) shot noise from Poisson photon-counting statistics (≤ 14 ppm), instrument noise (≤ 10 ppm), and stellar variability (≤ 10 ppm).[5] A major question raised by the first three Discovery review panels was whether CCDs could achieve an instrumental precision of 10 ppm or less, and further, whether a photometer composed of CCDs operating in a space-like environment could achieve this goal. After all, even though a telescope in deep space avoids the problems of peering up through the atmospheric soup surrounding the Earth, there are instrumental effects and noise even in the space environment. A series of laboratory measurements established that front-side illuminated CCDs can achieve the precision necessary for *Kepler*.[6] The arrival of readily available backside-thinned, illuminated CCDs brought the quantum efficiency of the proposed detectors to $> 90\%$, enhancing the prospects for *Kepler*, as this improvement significantly reduced the shot noise in measuring the brightness of star images. Laboratory studies with backside-illuminated CCDs demonstrated that they, too, could be operated in such a way as to achieve several ppm of instrumental noise on transit timescales,[7] and that they experienced less sub-pixel variations in sensitivity. Finally, the *Kepler* Technology Demonstration (KTD), funded and conducted after the 1998 Discovery proposal cycle, demonstrated that the *Kepler* design could reach the requisite instrumental precision in the face of a variety of disturbances of importance to a space-borne photometry mission.[8,9] These included residual pointing errors due to the rumble of reaction wheels used to control pointing and the band-limited performance of the attitude control system. Cosmic rays, bright, saturated stars in the field of view, and focus changes due to changing thermal conditions were also simulated. The KTD also provided direct simulations of Earth-size transit signals through the application of a small current through thin, ribbon wires placed across rectangular pinholes in the opaque plate that were imaged onto the test CCD[*], an EEV 42-80[†]. A few milliamperes of current heated the wires, causing them to expand by about one atom's width, thereby blocking $\sim$0.01% of the rectangular pinhole. The results allowed us to demonstrate that we could detect Earth-size transit signals against the shot noise and instrumental effects we knew would be at play in the space environment.

Second, the timescale and low duty cycle of transit signatures present serious challenges to Earth-bound transit photometry campaigns: a central transit of an Earth-size planet of a Sun-size star in an Earth-size orbit (1 AU) lasts for $\sim$13 hours, and repeats only once per year. It is difficult to imagine achieving measurements of a quality and continuity from

---

[*]An ingenious concept due to David Koch, Deputy Science Principal Investigator.

[†]The E2V CCDs built and flown on *Kepler* were derived from the EEV 42-80 CCD.

the ground required to reliably observe, let alone, detect transits of an Earth-size planet, even if the requisite photometric precision could be routinely obtained. It is true that prior to *Kepler*'s launch, ∼70 planets were found that transited their parent star. Almost all of these are at least as large or larger than Jupiter, providing transit depths of ∼1%, and in very short period orbits of only a few to several days. This set of circumstances allows for many transits during observing seasons lasting a few months, and transit durations lasting from one to a few hours, permitting detection from the ground. The fact that the stars can only be observed in visible wavelengths at night, the unpredictable nature of weather (which often interferes with astronomical observations), and the challenges in scheduling coordinated observations at multiple telescopes distributed around the globe all contribute to the difficulty of detecting habitable Earth-size planets from the ground [‡].

Third, the geometrical probability that the orbit of an extrasolar planet will be aligned so that we can observe its transits is small for an Earth-like orbit: the probability is the ratio of the size of the star to the size of the orbit. Thus, observers in our solar neighborhood have a 0.5% chance of seeing the Earth transit the Sun. This implies that for a robust null result, *Kepler* needs to observe thousands of stars in order to place strong upper limits on the frequency of such planets in the case that none are detected.

Fourth, we don't know when a star is going to dim due to a transit, and transits of terrestrial bodies transpire on timescales of 1–16 hours. The duty cycle of a transiting Earth-analog is only 0.15%. *Kepler* counts on building the SNR of a transit signature by combining together separate events and will be observing a handful of transits for Earth-analogs.

The solution to these challenges is to launch a photometer with a sufficiently sized aperture into a heliocentric, Earth-trailing orbit with a field of view large enough to observe a sample of ≥100,000 solar-like stars with instrumental "*Kepler*" magnitudes, Kp from 9 to 15 as continuously and contiguously as possible. [5,10] The design and build-up of the focal plane array, the largest ever built and launched by NASA, and the photometer itself were extremely challenging endeavors in the cost- and schedule-constrained aegis of NASA's Discovery Program. [11,12] *Kepler*'s Earth-trailing orbit provides a quiescent and stable environment in which to operate. The spacecraft's thermal environment is largely controlled by the measured and stately progress of the apparent position of the Sun moving along the ecliptic from *Kepler*'s point of view. The greatest force on the spacecraft is the torque due to the force of the photon pressure on the spacecraft and instrument. The Schmidt design of the photometer, a telescope with a 0.95-m aperture and a 1.4-m primary mirror, coupled with a focal plane that consists of 42 CCDs containing 94,617,600 pixels spanning 115 square degrees of sky, allow *Kepler* to simultaneously and nearly continuously observe ∼165,000 stars. The target stars were selected using the Kepler Input Catalog (KIC) to identify the stars for which we can most readily detect and confirm transits of small rocky planets. [13,14] The Attitude Determination and Control System (ADCS) provides extremely precise pointing with a required and delivered performance of *rms* pointing errors at the level of 0.009 arcsec, 3-σ on time scales upwards of 15 minutes. As the pixels span 3.98 arcsec on each side, this translates to pointing precision of 0.75 millipixels, 1-σ. This is ∼ 1000× better than that of the Hubble Space Telescope on a pixel scale. The compression scheme and the onboard storage allow *Kepler* to observe continuously for month-long intervals with brief interruptions to allow for downlinking the data to the ground.

The following sections describe some of the key challenges related to collecting and processing the science data and our efforts to mitigate them. Section 3 addresses the key challenge of monitoring the target stars as continuously as possible by minimizing both the number of planned interruptions to the observations as well as the time it takes to downlink the data from the spacecraft. Section 4 describes key challenges posed by nature in the form of stellar variability and by the subtle, but very important, thermal sensitivity of the instrument.

3. MANAGING *KEPLER'S* DATA VOLUME

One of the key challenges for *Kepler* is the management of the data volume. A full frame image (FFI) for *Kepler* has 101,744,160 pixels, including 7,126,560 collateral pixels used for calibration read out from 84 CCD module outputs (2 per CCD). The individual 6.54-sec frames are co-added for 29.4 minutes (a Long Cadence interval). Consequently, the full, uncompressed image data acquired every day are >300 GB. The full frame images contain significantly more data than we can afford to store onboard the Solid State Recorder (SSR), which must be able to hold at least two months of data for robustness against a missed monthly downlink opportunity. The strategy for reducing the data volume consists of first retaining only the pixels of interest (POI) and then applying a lossless compression scheme to squeeze out the

---

[‡]It appears to be impractical to detect Earth-size planets in the HZ of Sun-like stars by any means from the ground, given the small mass and size of such objects, which is why there are space missions proposed to detect them by transit, by ultra-high contrast imaging and by gravitational microlensing.
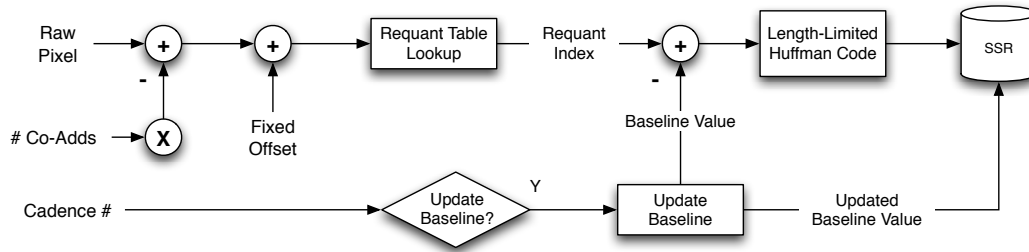
Figure 1. The flow of the compression algorithm implemented in flight software. The co-added pixel values are first shifted to a common zero point through the use of a fixed offset and the mean black level (bias). The shifted pixels are then mapped to the nearest neighbor in the requantization table that has larger steps between large pixel values and smaller steps between small pixel values so that the quantization noise is a fixed fraction of the intrinsic measurement uncertainty. A daily baseline value is subtracted and the residuals are entropically encoded using a length-limited Huffman code in order to squeeze out temporal redundancies in each pixel time series. The compressed bit stream is written to the Solid State Recorder for later downlink to the Deep Space Network.

temporal redundancies in the data stream. The responsibility for managing the data volume is distributed between the Science Operations Center (SOC) at NASA Ames Research Center, and *Kepler*'s flight software. The SOC provides the compression tables and the target definitions, and the flight software uses this information to select the pixel data that are compressed and stored on the SSR. The Data Management Center at STScI decompresses the data on the ground prior to sending them to the SOC. The success of this approach depends on a number of factors.

3.1 Discarding Pixels of Little or No Interest

The first step in reducing the data volume is accomplished through the use of target definitions, which allow us to specify up to 170,000 Long Cadence (LC) stellar targets for 29.4-minute integrations which can occupy up to 5,440,000 pixels. Each definition contains a reference row and column along as well as an index into an aperture mask table onboard *Kepler* containing 1024 different masks that vary in shape and size. [15] 512 Short Cadence (SC) targets with up to 43,520 pixels can also be specified for 58.7-sec integrations[§]. The KIC, together with models for the pointing behavior of the spacecraft and the point spread function (PSF), [16] allows us to identify the pixels required for each stellar target based on an SNR analysis of the average scene surrounding each target star. [15] More pixels are assigned to bright stars than to dim stars: LC targets are allocated an average of 32 pixels per star, while SC targets are allocated an average of 85 pixels per star. The aperture masks assigned to the targets don't contain much margin for error: a one-pixel halo is added to the pixels identified as essential to calibrating and making the photometric measurements. The masks are efficient: only 4% of the pixels addressed by the masks are not pixels of interest. [15] The POI include sufficient pixels to monitor the background flux levels (up to 4500 per CCD output) and to allow us to correct for on-chip artifacts such as variations in the bias voltage added to the CCD output prior to digitization, and to monitor and remove the effects of the shutterless readout smear which occurs because *Kepler* operates without a mechanical shutter. [17, 18] No background pixels are collected at SC, and the smear and black (bias) collateral data are only collected at the SC intervals for the rows and columns containing SC target pixels.

The success of this approach to reduce the amount of data stored and transmitted by *Kepler* relies on several factors. We need to understand in great detail the scene around each potential target star so that we can render accurate synthetic images for the SNR calculation supporting the identification of the required pixels. This is supplied by the KIC, which contains 4.5×10^6 stars and their characteristics[¶]. Generating the photometric scene for each target star requires knowledge of the PSF, and knowledge of exactly where the star is going to be throughout the three months of upcoming observations. The Pixel Response Function (PRF), essentially a 2-D representation of the interaction of the PSF with the sub-pixel sensitivity variations in the CCDs, allows the stellar images to be rendered accurately. How the celestial coordinates of the stars map to silicon coordinates is defined by the Focal Plane Geometry (FPG) model. These models are coupled to a heuristic, predictive model of the pointing behavior of the spacecraft in order to identify the POI. Obtaining the PRF and FPG models

---

[§]Each Long Cadence interval consists of 30 Short Cadence intervals, and each Short Cadence consists of 9 co-added 6.54-sec integrations.

[¶]Generating the KIC was a significant challenge in itself and required several observing seasons and a significant amount of effort to reduce the data and characterize the stars.

was a major feat and resulted from a set of unique data collected and analyzed during the commissioning phase. [16,19,20] A total of 121 15-minute LC frames were collected over a grid of 2-D offsets over ±0.5 pixels. These observations were made for 52,496 stars and used over-sized aperture masks with two halos to allow for uncertainties in the pre-launch FPG models. Approximately 200 of the brightest, unsaturated stars on each CCD readout channel were used to simultaneously solve for the super-resolution PRFs, which were allowed to vary in shape over each CCD readout channel, and for the FPG coefficients. The pointing model which plays an essential supporting role in these calculations assumes that once the ADCS locks onto the guide star, it acts to minimize the movement of the guide stars from their starting positions. This simple, heuristic pointing model has proven to be quite successful despite the fact that the detailed motion of the stellar images cannot be modeled by a static, rigid-body coordinate transform, due to small, thermally induced, non-uniform focus changes. The Target and Aperture Definition (TAD) pipeline component uses these models to analyze the average SNR of each target's flux measurement over the upcoming three months of observation. Note that differential velocity aberration causes the stars at the edges of the large $\sim 13.25° \times 13.25°$ field of view to move by up to ~0.6 pixels over 90 days so the aperture masks must be large enough to capture this motion.

Of equal importance to this task is the pipeline component, Photometer Data Quality (PDQ), which reconstructs the attitude of the spacecraft after each return to science data collection to confirm that each and every target star is within ±0.1 pixels or 0.398 arcsec of its expected location. [21] If we can't achieve this accuracy then the target definitions will become invalid during the observations and we lose essential data. This is a daunting task: the focal plane is approximately 12,000 pixels across. The required precision is therefore 1 part in 120,000. This is comparable to the photometric precision required to detect Earth-size transits. If any target star falls outside this very small bull's-eye, then PDQ furnishes a pointing "tweak" in the form of a delta quaternion that represents the error between the desired pointing and the actual pointing reconstructed from the data. Upon request by the *Kepler* Science Office, this delta quaternion can then be uplinked and injected into the ADCS as an artificial pointing error that will be nulled out and therefore, nudge the spacecraft to the correct attitude. PDQ itself has far fewer pixels to work with than is available for normal science, as its data is provided through the low gain antennas at X-band. At the start of the mission, PDQ relied on no more than 96,000 pixels with about 300 star images from the focal plane array, and now only has access to ~160 stars. The number of stellar targets that PDQ receives for its attitude reconstruction will continue to drop as it drifts away from Earth and the strength of the radio link to the spacecraft diminishes. So far, PDQ has proven itself up to the task.

The use of the target definitions reduces the fraction of pixels that are stored on the SSR to ~5% of that in a FFI. The raw data are represented as 23 bit words and the compressed data must occupy no more than 5.75 bits per pixel on average in order for the SSR to achieve adequate storage capacity. The uncompressed POIs are still a factor of 4 too large to store on the SSR. We can take advantage of two aspects of the digitized data to achieve the necessary level of compression: 1) the digitized pixel data for bright pixels are highly over-represented, and 2) the temporal redundancy in the observations. The former is handled by the requantization scheme described in Section 3.2, and the latter is addressed by a length-limited Huffman code discussed in Section 3.3.

3.2 Requantization

First, the 14-bit Analog-Digital-Converters (ADC) quantize the pixel measurements uniformly to $\approx 100\,e^-/\text{ADU}$, regardless of the intrinsic measurement noise of each observation. As a consequence, the bright pixels are over-represented due to shot noise, which varies as the square root of the number of photons as an *rms* value. For example, the well depth of the CCDs is approximately $1 \times 10^6\,e^-$. Thus, after 270 exposures (an LC interval), the brightest pixels have $270 \times 10^6\,e^-$ with a corresponding shot noise of $1{,}6432\,e^-$, and the quantization is at the $100\,e^-$ level,[22] so these pixels have a resolution that is 164 times smaller than the intrinsic measurement uncertainty. To reduce the degree to which bright pixels are over-represented, *Kepler* applies a software "compander" to redistribute the bits associated with the pixel measurements so as to make the ratio of the quantization noise to the total intrinsic noise a fixed value chosen to be $r = ¼$, called the requantization ratio. This is accomplished with a "requantization" table that is a list of allowed pixel values whose spacing increases as a function of the measured pixel value. The requantization algorithm replaces each pixel measurement with the index of the nearest pixel value in the requantization table (containing exactly 2^{16} entries) by the flight software, i.e., it is a simple look-up table with nearest neighbor interpolation.

What effect does requantization have on the total noise? We have

$$\sigma_{\text{total}}^2 = \sigma_{\text{intrinsic}}^2 + \Delta_Q^2/12 = \sigma_{\text{intrinsic}}^2 + r^2\,\sigma_{\text{intrinsic}}^2 = \left(1 + r^2\right)\,\sigma_{\text{intrinsic}}^2 \tag{1}$$
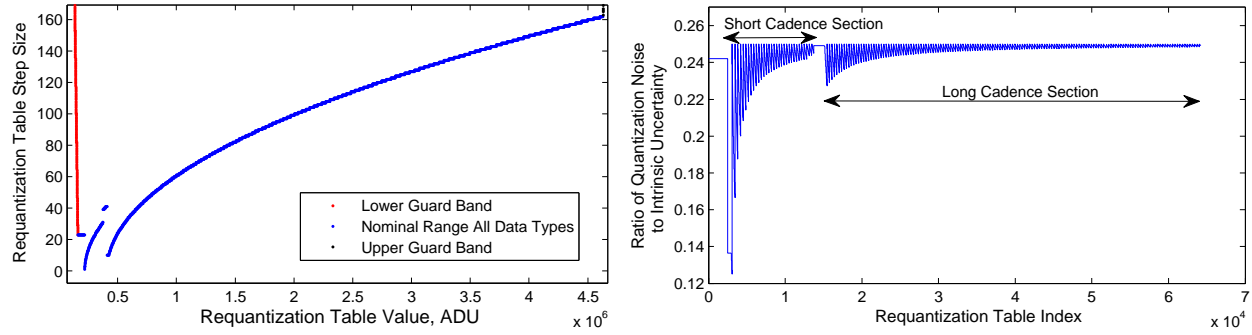
Figure 2. Left: The requantization table step sizes as a function of table index. The two main photometric data sections are shaped approximately like the square root function, with low middle and high guard band sections above, below and in between the short cadence and long cadence sections of the table. Right: A verification figure showing that all data types are quantized to no more than ¼ of their intrinsic uncertainties.

where σ^2_{total} is the combination of the measurement uncertainty, $\sigma^2_{\text{intrinsic}}$, and the quantization noise, $\Delta^2_Q/12$, due to a quantization step size of Δ_Q.[23] The requantization increases the *rms* noise on the observations by $\sigma_{\text{total}}/\sigma_{\text{intrinsic}} - 1 = \sqrt{1 + r^2} - 1 = 0.03$ for the choice $r = ¼$ a rather modest increase of 3%. This is acceptable as this approach treats the quantization noise as a term in the noise budget and the requantization scheme allows us to trade a slight increase in the noise level of the photometric measurements for a large reduction in the data volume taken up by the measurements and the time required to downlink the data.

How do we build the requantization table? The concept is simple: start with the lowest photoelectron count expected in terms of digital counts, p_{min}, and set the first value in the requantization table, p_1 to this value. Set the counter $i = 1$. The intrinsic uncertainty in a pixel value, p_i, in ADU is given by

$$\sigma^2_{p_i} = (p_i - n_{\text{co-adds}} \cdot \mu_{\text{black}})/G_j + n_{\text{co-adds}} \cdot \sigma^2_{\text{read}}, \tag{2}$$

where $n_{\text{co-adds}}$ is the number of individual exposures that were summed to obtain the pixel value, including any spatial co-adds, μ_{black} is the mean black or bias level in ADU, G_j is the gain (ADU/e⁻) for the CCD channel j, and σ_{read} is the *rms* read noise in ADU (typically 1 ADU). Compute the step size for element, i, as

$$\Delta_Q(p_i) = \max\left\{1, \left\lfloor \sqrt{12}\, r\, \sigma_{p_i} \right\rfloor\right\}, \tag{3}$$

where $\lfloor \cdot \rfloor$ is the floor operator. Then $p_{i+1} = p_i + \Delta_Q(p_i)$.

In practice, generating the requantization table for the flight segment is complicated by the fact that the bias voltages added to the CCD readouts vary significantly across the focal plane, and they vary spatially even within each CCD readout channel.[22] The SOC furnishes a mean black table to the flight segment for this use in addition to the requantization table. The electronic gains also vary significantly over the 84 CCD readout channels.[22] Moreover, the collateral data used to calibrate the photometric data for on-chip artifacts, such as the bias voltage (or black level) and the shutterless readout smear, are co-added spatially before being compressed. Also, there are two cadences for photometric data, Short Cadence, consisting of 9 summed readouts, and Long Cadence, consisting of 270 summed CCD readouts. The readout noise associated with SC and LC are quite different for pixels having the same value. Because of this, it is advantageous to design separate requantization table sections for the SC and LC data to help maximize the compressibility of the resulting data. The SOC generates a table combining the LC and SC sections, and uses a LC fixed offset of 419,400 ADU, and a SC fixed offset of 219,400 ADU that allow the flight software to tailor the requantization to the cadence type for each pixel measurement. Generating the requantization table requires a bit of bookkeeping.

Equations 2 and 3 are exercised for each table section to calculate the step size required by each SC or LC data type across the focal plane. The step size taken is the smallest one required, after which the process repeats until p_i exceeds the expected range of the photometric measurements. This design allows for guard bands above, below, and between the two main requantization tables to ensure that drifts in the DC bias voltages don't result in variations in pixel values that fail to be captured by the requantized data because the input values fall outside the expected input range. Requantization reduces the size of the data from 23 bits to 16 bits per pixel per cadence, a substantial, but insufficient reduction in the data volume.
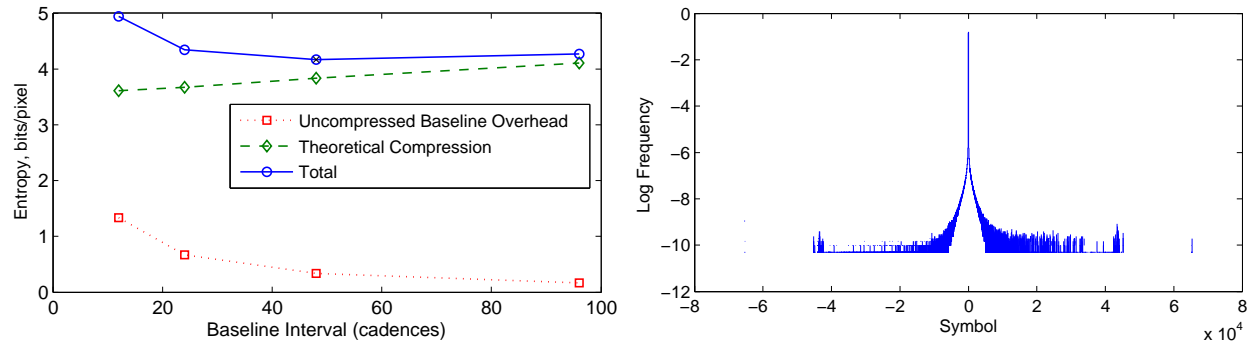
Figure 3. Left: The compression rate as a function of the baseline interval for the predictor for four different baseline intervals. The solid blue curve with circles is the total compression rate, while the dashed green curve with diamonds is the entropy for the compressed data and the dotted red curve with squares is the overhead cost associated with storing the baselines, which are not compressed. There is a shallow minimum at 48 cadences ($\sim$ 1 day), which is the value selected for the baseline interval. Right: Histogram of the symbol frequencies corresponding to a baseline interval of 48 Long Cadences. The symbols can span the range from $-2^{16} + 1$ to $2^{16} - 1$. The compactness of the residuals dictates the compression that can be achieved. Over 99% of the pixel residuals are expected to be within 13 requantization levels of the daily baseline value.

3.3 Length-Limited Huffman Coding

The second part of the compression scheme takes advantage of the slowly varying nature of the scene imaged by *Kepler* to reduce the variance in each POI's time series by removing a predicted value for each POI. This prediction is furnished by a requantized measurement for each pixel made during a baseline cadence interval, and this baseline measurement is updated every 48 cadences (which is a software parameter) starting with the first cadence collected after return to science mode. The residuals from the baseline value are entropically encoded using a length-limited Huffman code [24–26] that limits the code words to no more than 24 bits. Huffman codes compress data streams by representing common symbols with short binary code words and uncommon symbols with long code words [‖]. Length-limited Huffman codes are somewhat less efficient than non-length-limited codes, but the performance in the context of *Kepler* is more than adequate. The uncompressed baseline pixel values are stored onboard the SSR as well as the differences between the previous baseline value and the new baseline value for each pixel, which is compressed. This allows us to reconstruct the requantized pixel values from the bit stream both forward from the previous baseline as well as backwards from the following baseline in case a baseline measurement is lost or corrupted.

Generating a Huffman coding table requires that the frequencies of the symbols to be coded be quantified. In *Kepler*'s case, we needed to generate and fly a compression table prior to flight for test purposes. To do so, we generated high fidelity, synthetic science data using the *Kepler* End-To-End Model (ETEM) [27, 28] and ran it through the Huffman Generator (HGN) pipeline where the the symbol histograms are generated for each of the 84 CCD readout channels [**] for the list of baseline intervals specified on input. The Huffman Accumulator (HAC) pipeline then aggregated the results across the 84 module outputs and produced diagnostic plots and information so that we could determine whether the default baseline cadence interval produced adequate compression rates. Figure 3 shows that the default baseline interval of 48 Long Cadences is located approximately at the bottom of a very shallow minimum as the overhead associated with storing the uncompressed baseline interval data is traded against better compression for shorter baseline intervals. The predicted compression rate is 4.17 bits per pixel, which is significantly better than the requirement.

The original plan was to update the Huffman table once we were in orbit and had the opportunity to collect a sufficient amount of flight data. However, as the data in Figure 4 shows, this was not necessary. The Calibration (CAL) pipeline examines the original LC pixels that flow through it to be calibrated and calculates the achieved and theoretical entropies for tracking and trending purposes. [29] As can be seen for the third quarter of observations (Q3), the difference between the achieved and theoretical entropies is only 0.13 bits per symbol, or 3%, so in spite of the fact that ETEM does not simulate

---

[‖]Huffman codes are ubiquitous and are used in various digital coding standards including mp3 and jpeg applications as well as in fax machines.
[**]Each CCD has two readout channels, or module outputs.
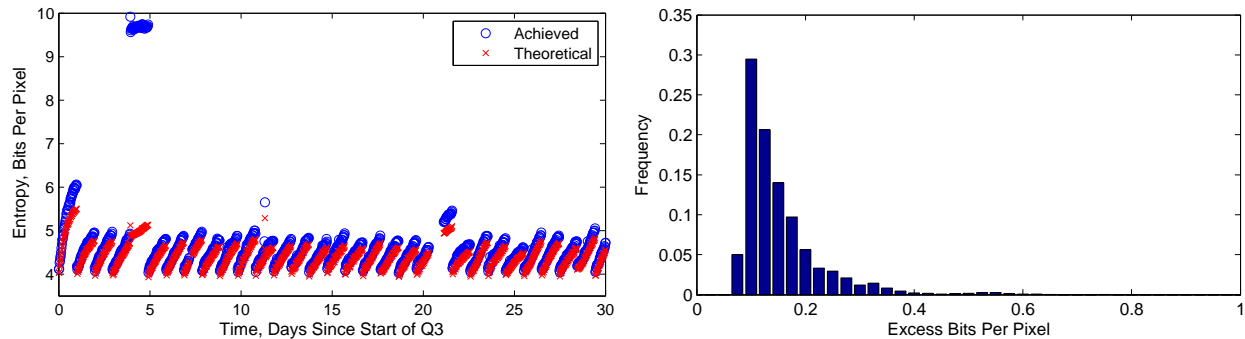
Figure 4. Left: Achieved and theoretical compression rates for the Q3 data set for the first 30 days of the data collection period. This data set spanned ∼90 days and was the first "typical" quarter of observations as it was 3 months long and did not suffer from excess pointing drift, which necessitated pointing "tweaks" during Q2, or from excessive safe mode events. The effect of the predictor chosen for *Kepler* can be seen in the ramping up of the entropies over the course of each 48-cadence interval (≈1 day) as the baseline values for each pixel go stale. There are some occasions when the baseline is anomalous, most likely due to an Argabrightening event when a piece of debris crosses the aperture and reflects light into the barrel of the telescope.[30] Right: Histogram of the differences between the achieved and the theoretical compression rates given the distribution of requantized pixel residuals. The median achieved compression rate is 4.4 bits per pixel, only 0.13 bits per pixel above the theoretical minimum for a perfectly tuned compression table. The achieved compression is within 3% of the theoretical minimum for the chosen compression algorithm.

highly variable, non-solar-like stars, of which there are several thousand to be found in the *Kepler* target catalog, we are achieving a level of compression, ∼4.4 bits per pixel per cadence, that is very close to the optimum for the compression algorithm selected and implemented in flight and ground software.

4. CHALLENGES TO PHOTOMETRIC PRECISION

Since launch, *Kepler* has provided photometric time series of unprecedented quality and completeness which have in many respects surpassed the expectations of the scientists and engineers who designed and built the spacecraft. There have been some important facts that came to light after *Kepler* returned a significant amount of data. First, while the photometry has been unparalleled in quality, there appears to be excess photometric noise so that the mode of the precision for $Kp = 12$ G2V stars (solar analogs) on timescales of 6.5 hours is 30 ppm rather than the desired goal of 20 ppm. The *Kepler* team has been studying the data to identify likely causes and has determined that the bulk of the increase in the observed photometric noise is due to stellar variability,[31] which is about twice as high as expected based on *SOHO* observations of the Sun.[3] This is an important discovery, both from the standpoint of understanding our Sun in the context of stars in general, and from that of designing future space transit photometry missions.

The fact that solar-like main-sequence stars exhibit more variability than the Sun on timescales relevant to transit detection does not prevent the *Kepler Mission* from achieving its goals, as increasing the duration of the mission to a period of 8 years will recover the originally scoped sensitivity. However, it does make it that much more important to deal with other challenges facing the attainment of 20 ppm photometric precision, such as various systematic errors and instrumental signatures, which are not always adequately removed from *Kepler* light curves at present.

4.1 Instrumental Signatures and Systematic Errors

Although *Kepler* is in a very benign, Earth-trailing orbit, there are changes in the thermal state of the telescope as the Sun moves in relation to the telescope. There are also heaters on various spacecraft components used to condition the temperatures of these items within their required bounds. The telescope changes shape in response to the changing distribution of temperatures in the structure, and consequently, the focus of the instrument changes in subtle, but important ways.[17,32] In fact, during the first quarter of science observation we noticed that a heater in the reaction wheel assembly for wheels 3 and 4 was cycling on and off in response to the fact that the box was becoming more shaded during the quarter and the changing temperature of the box was inducing perfectly correlated signatures in the science data at the pixel level. The shape of the telescope was deforming and changing the distance between the primary mirror and the focal plane assembly by ∼1 μm in response to this heater. This is a very small change in the state of the telescope, but when the goal is to reach
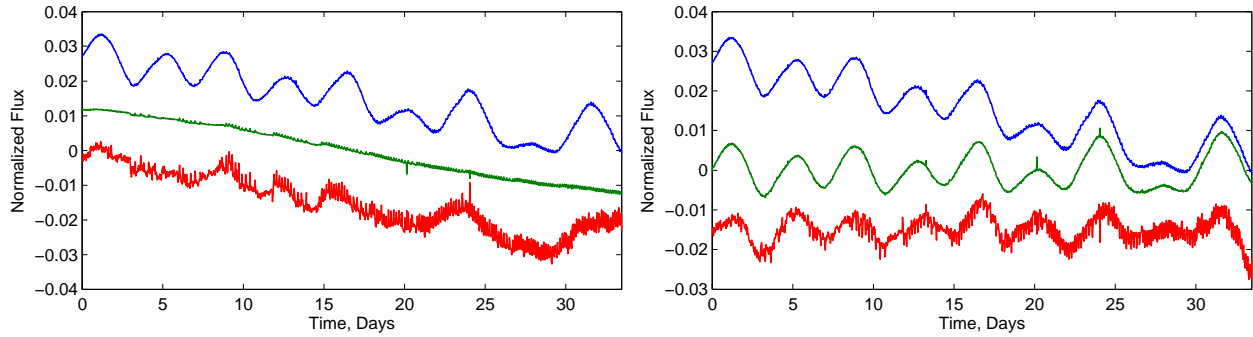
Figure 5. Light curves for one target on the most thermally sensitive CCD channel 2.1 in the *Kepler* focal plane for the Q1 observations. Left: The top curve (blue) is the simple aperture photometry flux time series, the middle (green) curve is the result of a MAP fit with Gaussian priors, and the bottom (red) curve is the result of a robust fit to the same basis vectors. Right: The top (blue) curve is the original flux, the middle (green) curve is the MAP-corrected flux, and the bottom (red) curve is the robust least-squares-corrected flux time series.

a photometric precision of 20 ppm, it is a significant change. The temperature limits of the thermostat were tightened up so that the cycle time was shortened below one half hour and the temperature swing was significantly reduced.

In the SOC Pipeline, the Pre-search Data Conditioning (PDC) module's task is to remove systematic errors from the raw flux time series.[33] These include telescopic and spacecraft effects such as pointing errors, focus changes, and changing instrument properties. PDC co-trends each flux time series against ancillary engineering data, such as temperatures of the focal plane and electronics, pointing history, and focus variations, to remove signatures correlated with systematic errors. In general, PDC is doing a good job of correcting systematics for quiet, main-sequence stars, but it is not performing a uniformly good job for all targets, especially for those exhibiting significant intrinsic stellar variability. In some cases PDC removes or grossly distorts intrinsic variations and/or introduces short timescale variations that effectively add noise to the light curves, making it more difficult to detect signatures of transiting planets or to study astrophysics. We also see that in many cases the output light curves from PDC exhibit significant cross correlations, indicating that PDC is not removing all the instrumental signatures and systematics exhibited by the light curves. The basic problem is that PDC is fitting an incomplete model to the data and a maximum likelihood (ML) approach is happy to trade a reduction in bulk *rms* at the cost of introducing excess power on shorter time scales: ML is able to find a happenstance linear combination of basis vectors that match the gross profile of intrinsic stellar variations.

The solution we are implementing is a Bayesian Maximum A Posteriori (MAP) approach whereby we learn about the influence of the systematic errors by examining the behavior of the ensemble of light curves on each CCD readout channel.[34] Figure 5 shows the results of applying a simple version of MAP to Q1 data when the heater on the reaction wheel assembly was active. We performed a singular value decomposition of the most-correlated light curves on this channel to obtain 10 basis vectors that were then robustly fitted to each stellar light curve. We formulated analytical priors from the distributions of the fit coefficients for each term and then applied a MAP fit. The MAP fit was able to "put the brakes" on the least-squares model fit so that highly variable stars were not over-fitted in an attempt to reduce the bulk *rms*, and intrinsic stellar variability was preserved to a high degree while instrumental systematics, such as a long term change in focus that reduced the brightness of the stars, and short term variations in focus caused by the reaction wheel heater, were effectively removed from the light curves. An empirical version of MAP is being implemented in the SOC PDC pipeline and will be completed and running on *Kepler* data sets by the end of 2011. We expect PDC-MAP to deliver light curves of much higher quality for asteroseismology and astrophysics investigations and for the exoplanet search.

5. KEY SCIENCE RESULTS

The *Kepler Mission* has been generating exciting science results right out of the box. The 10 days of continuous observations at the end of commissioning, now dubbed Q0, or Quarter 0, made it clear that detecting transits of giant planets was accomplished easily by eye. Examination of the light curve for HAT-P-7b revealed an ≈100 ppm drop in brightness 180 ° out of phase (an occultation) with the 0.6% transits that had been detected from the ground in 2008 before *Kepler* was launched.[35] These small dips are the signature of the atmosphere of the planet heated to ≈2600 K by its proximity to its

xix

star, and were accompanied by phase variations in the light curve indicating that the transport of heat from the dayside to the nightside of the planet is inefficient.[36] This light curve demonstrated unambiguously that *Kepler* can detect transiting planets and furthermore, can detect the weak signatures of Earth-like planets transiting sun-like stars.

The identification of hundreds of potential transiting planets in the initial *Kepler* observations followed quickly on the heels of the occultation of HAT-P-7b. By January of 2010, five planets were announced and hundreds of additional candidates awaited the following observing season for follow up observations and confirmation. The first system of multiple transiting planets was announced in August 2010,[37] consisting of two Saturn-size planets conducting a coupled orbital dance near resonance with 19.24 and 38.91 day periods. These bodies exhibit mutual gravitational interactions in the timing of the transits observed by *Kepler*. These transit timing variations (TTVs) can be used to infer or constrain the masses of the transiting bodies, and can also indicate the presence of non-transiting planets that are perturbing the orbits of the transiting planets. The first unquestionably rocky planet was announced by the *Kepler* team in January of 2011.[38] Radial velocity observations of this planet indicated it has a mass of 4.5 $M_\oplus$, so with a radius of 1.4 $R_\oplus$ this planet has a density of 8.8 g cm^{-3}. Asteroseismology provided a much improved radius estimate for Kepler-10b's star. Kepler-11, an extremely compact system of 6 transiting planets, was discovered with 5 of the 6 planets exhibiting TTVs so that their masses could be estimated directly from the *Kepler* data.[39] The planetary orbits in this system are highly coplanar.

Beyond the individual planet discoveries, the statistics of the *Kepler* results are accumulating to the point that we are learning about the nature and prevalence of planetary formation. Of the 1235 candidates identified by *Kepler*,[1] 408 of these planetary candidates are found in 170 multiple systems, demonstrating the flatness of planetary systems composed of small planets. Analysis of the single transiting candidates and the multiple transiting candidates suggests a relative absence of giant planets in close orbits for the multiple planet systems, and that the false positive rate for the multiple transit systems is significantly lower than that of the single transit planet candidates.[40] The data release of February 2011 has led to a profusion of papers inferring the intrinsic planet frequency from the initial candidate planet catalog. While it is premature to extrapolate these initial findings to the ultimate prize, Earth-size planets orbiting in the habitable zone of solar-like stars, the initial results indicate that the frequency of planets varies inversely with their size, so that smaller planets are more common than giant planets down to at least 2 $R_\oplus$.[1,41]

As important as *Kepler* is for exoplanets, the asteroseismology community in turn is using this instrument as a near-ideal platform to write new chapters in their field. Initial results from the *Kepler* data suggest that the long-held belief that asteroseismology can reveal the secret inner workings of stars is being confirmed today.[42] The *Kepler* data allow us to quantify global properties of the observed stars, such as radius and age, through observations of normal modes of oscillation. One of the most exciting recent results is the ability of *Kepler* to distinguish between giant stars that are still burning hydrogen in a shell surrounding the accumulating helium core, and those giants that have initiated helium burning in the core.[43] Finally, the *Kepler* data are also being used to study a wide variety of oscillating and pulsating stars, including RR Lyr stars, which can more than double their brightness every 12 hours, as well as cataclysmic variable stars.

6. CONCLUSIONS

The *Kepler* Mission is solving an astonishing array of astrophysical mysteries with its unprecedented photometric precision and near continuous observations. The success of *Kepler* is the result of many years of hard work and effort on the part of the thousands of individuals who contributed to the design, implementation, and operation of the instrument and spacecraft and of those who process and analyze the resulting data. Twenty-five years ago the *Kepler* concept was a sci-fi fantasy that only a few individuals, notably the Science Principal Investigator, William J. Borucki, believed in. The protagonists in this narrative persevered and overcame the many daunting obstacles in the path to the ultimate goal by meeting each challenge as it arose and mustering the resources and talent to solve each problem in turn.

By their nature, transit survey missions rely on collecting time series image data. Such missions must rely on the stability of their observing platforms to achieve the ultra high precision needed to discover small planets. The methodology used by *Kepler* to reduce the data volume to a manageable level, and then to compress the data without loss can be readily applied to future missions to reduce the storage required per sample and to minimize the transmission time required to downlink the original data. It is extremely important to minimize the perturbations to the instrument on timescales from 0.01 to several days. Even in *Kepler*'s benign orbital environment, identifying and removing instrumental systematic errors is a real challenge for such sensitive instruments, and the innovative use of Bayesian methods should be explored.

ESA's PLATO Mission,[44] an ambitious transit survey to discover Earth-size planets around the closest and brightest main-sequence stars may be selected for flight by the end of 2011. It would launch in 2017 or 2018 into an orbit at L2 to survey several large $> 800 \deg^2$ fields of view with an instrument composed of ~ 30 small telescopes. Also, at least two transit surveys have been proposed to NASA's current Explorer Mission competition. MIT has proposed the Transiting Exoplanet Survey Satellite (TESS) mission,[45] an optical, all-sky transit survey satellite to be launched into orbit in 2016 for a two-year mission with an instrument composed of multiple telescopes with disjointed fields of view. JPL has also proposed an infrared transit survey mission called ELEKTRA to the Explorer Program. [46] These future missions will face many of the same challenges and will surely benefit from the successes of and the lessons learned from the *Kepler Mission*.

ACKNOWLEDGMENTS

REFERENCES

[1] Borucki, W. J.,*et al.*, "Characteristics of planetary candidates observed by *Kepler*. II. Analysis of the first four months of data," ApJ 736(1), 19 (2011).

[2] Jenkins, J. M., D. A. Caldwell, and Borucki, W. J., "Some tests to establish confidence in planets discovered by transit photometry," ApJ 564, 495 (2000).

[3] Jenkins, J. M., "The impact of stellar variability on the detection of transiting terrestrial planets", ApJ 575, 493 (2002).

[4] Young, A. T., "Photometric error analysis. VI. Confirmation of Reiger's theory of scintillation," AJ 72, 747–753 (1967).

[5] Koch, D. G., *et al.*, "*Kepler Mission* design, realized photometric performance, and early science," ApJL 713(2), L79–L86 (2010).

[6] Robinson, L. B., Wei, M. Z., Borucki, W. J., Dunham, E. W., Ford, C. H., and Granados, A. F., "Test of CCD Precision Limits for Differential Photometry," PASP 107, 1094 (1995).

[7] Jenkins, J. M., Borucki, W. J., Dunham, E. W. and McDonald, J. S., "High Precision Photometry with Back-Illuminated CCDs," ASP Conf. Ser., 119, 227–280 (1997).

[8] Koch, D. G., *et al.*, "CCD photometry tests for a mission to detect Earth-size planets in the extended solar neighborhood," Proc. SPIE 4013, 508–519 (2000).

[9] Jenkins, J. M., Witteborn, F., Koch, D. G., Dunham, E., Borucki, W. J., Updike, T. F., Skinner, M. A., and Jordan, S. P., "Processing CCD images to detect transits of Earth-sized planets: Maximizing sensitivity while achieving reasonable downlink requirements," Proc. SPIE 4013, 520–531 (2000).

[10] Borucki, W., *et al.*, "*Kepler* planet-detection mission: introduction and first results," Science 327, 977–980 (2010).

[11] Ebbets, D., Atcheson, P., Stewart, C., Spuhler, P., "Optical performance of the 100 sq deg FOV telescope for NASA's *Kepler* exoplanet mission," Proc. SPIE 8146, 8146-15, this volume (2011).

[12] Ebbets, D., Argabright, V., VanCleve, J., Caldwell, D. "In-flight performance of the 96 Mpx focal plane for NASA's *Kepler* mission," Proc. SPIE 8146, 8146-16, this volume (2011).

[13] Batalha, N. M., *et al.*, "Selection, prioritization, and characteristics of *Kepler* target stars," ApJL 713(2), L109-L114 (2010).

[14] Brown, T. M., Latham, D. W., Everett, M. E., and Esquerdo, G. A., "*Kepler* input catalog: Photometric calibration and stellar classification," AJ, in press, arXiv:1102.0342 (2011).

[15] Bryson, S. T., *et al.*, "Selecting pixels for *Kepler* downlink," Proc. SPIE 7740, 77401D (2010).

[16] Bryson, S. T., *et al.*, "The *Kepler* pixel response function," ApJL 713(2), L97–L102 (2010).

[17] Jenkins, J. M., *et al.*, "Overview of the *Kepler* science processing pipeline," ApJL 713(2), L87-L91 (2010).

[18] Quintana, E. M., *et al.*, "Pixel-level calibration in the *Kepler* Science operations center pipeline," Proc. SPIE 7740, 77401X (2010).

[19] Tenenbaum, P., and Jenkins, J. M., "Focal plane geometry characterization of the *Kepler Mission*" Proc. SPIE 7740, 77401C (2010).

[20] Haas, M., *et al.*, "*Kepler* science operations," ApJL 713(2), L115–L119 (2010).

[21] Chandrasekaran, H., *et al.*, "Semi-weekly monitoring of the performance and attitude of *Kepler* using a sparse set of targets," Proc. SPIE 7740, 77401B (2010).

[22] Van Cleve, J., and Caldwell, D. A., [*Kepler* Instrument Handbook, KSCI 19033-001], NASA Ames Research Center, Moffett Field, CA (2009).

[23] Papoulis, A., [Probability, Random Variables, and Stochastic Processes], McGraw Hill, New York (1984).

[24] Huffman, D. A., ""A Method for the Construction of Minimum-Redundancy Codes," Proc. Inst. Radio. Eng. 40, 1098-1101 (1952).

[25] Larmore, L. L., and Hirschberg, D. S. , "A fast algorithm for optimal length-limited Huffman codes", J. Assoc. Comput. Mach. 37(3), 464–473 (1990).

[26] Katajainen, J., Moffat, A., and Turpin, A., "A fast and space-economical algorithm for length-limited coding", Proc. of the 6th Int. Symp. on Algorithms and Computation, 1004, 12 – 21 (1995).

[27] Jenkins, J. M., Peters, D. J., and Murphy, D. W., "An efficient end-to-end model for the *Kepler* photometer," Proc. SPIE 5497, 202-212 (2004).

[28] Bryson, S. T., Jenkins, J. M., Peters, D. J., Tenenbaum, P. P., Klaus, T. C., Gunter, J. P., Cote, M. T., and Caldwell, D. A., "The *Kepler* end-to-end model: creating high-fidelity simulations to test *Kepler* ground processing," Proc. SPIE 7738, 773808 (2010).

[29] Li, J., *et al.*, "Photometer performance assessment in *Kepler* science data processing," Proc. SPIE 7740, 77401T (2010).

[30] Witteborn, F. C., Van Cleve, J., Borucki, W. J., Argabright, V. S., and Hascall, P., " Debris sightings in the Kepler field," Proc. SPIE 8151, 8151-42 (2011).

[31] Gilliland, R. L., *et al.*, "*Kepler Mission* stellar and instrument noise properties," ApJ, in press, arXiv:1107.5207 (2011).

[32] Jenkins, J. M., *et al.*, "Initial characteristics of *Kepler* long cadence data for detecting transiting planets," ApJL 713(2), L120-L125 (2010).

[33] Twicken, J. T., Chandrasekaran, H., Jenkins, J. M., Gunter, J. P., Girouard, F., Klaus, T. C., "Presearch data conditioning in the *Kepler* science operations center pipeline," Proc. SPIE 7740, 77401U (2010).

[34] Jenkins, J. M., Smith, J. C., Tenenbaum, P., Twicken, J. T., "Planet detection: the *Kepler Mission*," [Advances in Machine Learning and Data Mining for Astronomy], Chapman and Hall/CRC Press, in press (2011).

[35] Pál, A., *et al.*, "HAT-P-7b: An extremely hot massive planet transiting a bright star in the *Kepler* field," ApJ 680(2), 1450-1456 (2008).

[36] Borucki, W. J., *et al.*, "*Kepler*'s optical phase curve of the exoplanet HAT-P-7b," Science 325, 709 (2009).

[37] Holman, M. *et al.*, "Kepler-9: A system of multiple planets transiting a sun-Like star, confirmed by timing variations,", Science 330, 51 (2010).

[38] Batalha, N. M., *et al.*, "*Kepler*'s first rocky planet: Kepler-10b," ApJ 729, 27 (2011).

[39] Lissauer, J. J., *et al.*, "A closely packed system of low-mass, low-density planets transiting Kepler-11," Nature 470, 53–58.

[40] Latham, D., *et al.*, "A first comparison of *Kepler* planet candidates in single and multiple systems," ApJL 732, L24 (2011).

[41] Howard, A. W., *et al.*, "Planet occurrence within 0.25 AU of solar-type stars from *Kepler*" ApJ, arXiv:1103.2541 (2011).

[42] Gilliland, R. L., *et al.*, "*Kepler* asteroseismology program: Introduction and first results," PASP 122, 131–143 (2010).

[43] Bedding, T. R., *et al.*, "Gravity modes as a way to distinguish between hydrogen- and helium-burning red giant stars," Nature 471, 608-611 (2011).

[44] Claudi, R., "A new opportunity from space: PLATO mission," Ap&SS 328, 319–323 (2010).

[45] Ricker, G., *et al.*, "Transiting Exoplanet Survey Satellite (TESS)," BAAS 42, 459 (2010).

[46] Beichman, C. and the ELEKTRA Team, "The ELEKTRA explorer mission to find transiting earth like planets," presented at the Strange New Worlds Conference held in Flagstaff AZ (2011).

Large Binocular Telescope Adaptive Optics System:
New achievements and perspectives in adaptive optics

S. Esposito*[a], A. Riccardi[a], E. Pinna[a], A. Puglisi[a], F. Quirós-Pacheco[a], C. Arcidiacono[a],
M. Xompero[a], R. Briguglio[a], G. Agapito[a], L. Busoni[a], L. Fini[a], J. Argomedo[a], A. Gherardi[a],
G. Brusa[b], D. Miller[b], J. C. Guerra[b], P. Stefanini[a], P. Salinari[a]

[a]INAF - Osservatorio Astrofisico di Arcetri, Largo E. Fermi 5, 50125 Firenze, Italy;
[b]LBT Observatory, Univ. of Arizona, 933 North Cherry Ave., Tucson AZ 85721, USA

ABSTRACT

The Large Binocular Telescope (LBT) is a unique telescope featuring two co-mounted optical trains with 8.4m primary mirrors. The telescope Adaptive Optics (AO) system uses two innovative key components, namely an adaptive secondary mirror with 672 actuators and a high-order pyramid wave-front sensor. During the on-sky commissioning such a system reached performances never achieved before on large ground-based optical telescopes. Images with 40mas resolution and Strehl Ratios higher than 80% have been acquired in H band (1.6 μm). Such images showed a contrast as high as 10^{-4}. Based on these results, we compare the performances offered by a Natural Guide Star (NGS) system upgraded with the state-of-the-art technology and those delivered by existing Laser Guide Star (LGS) systems. The comparison, in terms of sky coverage and performances, suggests rethinking the current role ascribed to NGS and LGS in the next generation of AO systems for the 8-10 meter class telescopes and Extremely Large Telescopes (ELTs).

Keywords: Large Binocular Telescope, high-order adaptive optics, pyramid sensor, adaptive secondary mirror.

1. INTRODUCTION

The purpose of Adaptive Optics (AO) is to correct wave-front aberrations of the electromagnetic waves received from a ground-based telescope after propagation through the atmosphere obtaining an image quality reached otherwise only with space-based telescopes. The Large Binocular Telescope[1] (LBT) features two 8.4m optical trains, each one of them fully integrated with AO correction provided by the two Adaptive Secondary Mirror (ASM) units with 672 actuators. The First-Light AO (FLAO) system[2], designed for each optical train, is a Natural Guide Star (NGS) AO system featuring a modulated pyramid Wave-Front Sensor (WFS) with a maximum pupil sampling of 30×30 subapertures. A so fine spatial sampling is new for astronomical AO typically working in a photon starving regime. The spatial sampling is difficult to be realized also because of the technical limitations imposed by the limited degrees of freedom available on wave-front correctors. In the compromise between correction performance and available light, the efficiency of wave-front sensors plays a dominant role. In our system, the use of state-of-the-art devices such as the pyramid WFS and the adaptive secondary mirror offers the optimal playground for very high Strehl Ratio (SR) corrections on the bright end, and high efficiency use of reference starlight photons on the faint one. As we will show in this paper, we have obtained >80% correction @ 1.6 μm on a bright star (up to M_R~9), and closed efficiently the loop on a ~17th magnitude star with ~15 photons per subaperture per frame (~500 in the whole pupil).

The on-sky commissioning of the FLAO#1 system (installed on the right side of the telescope) started in May 2010 and will be completed in the fall of 2011. The installation of the FLAO#2 system on the left side of the telescope started in August 2011. The two FLAO systems will provide AO correction on the bent-Gregorian focal stations serving the LUCIFER spectro-imagers[4].

We will present in this paper the on-sky performance analysis of the FLAO#1 system based on the data collected during the commissioning nights. After a brief system overview, we will present and discuss in the paper the performance achieved during the commissioning campaign. Finally we will present some considerations for future AO systems based on the results achieved at LBT.

*esposito@arcetri.astro.it; phone +39 055 2752 309; fax +39 055 2752 292
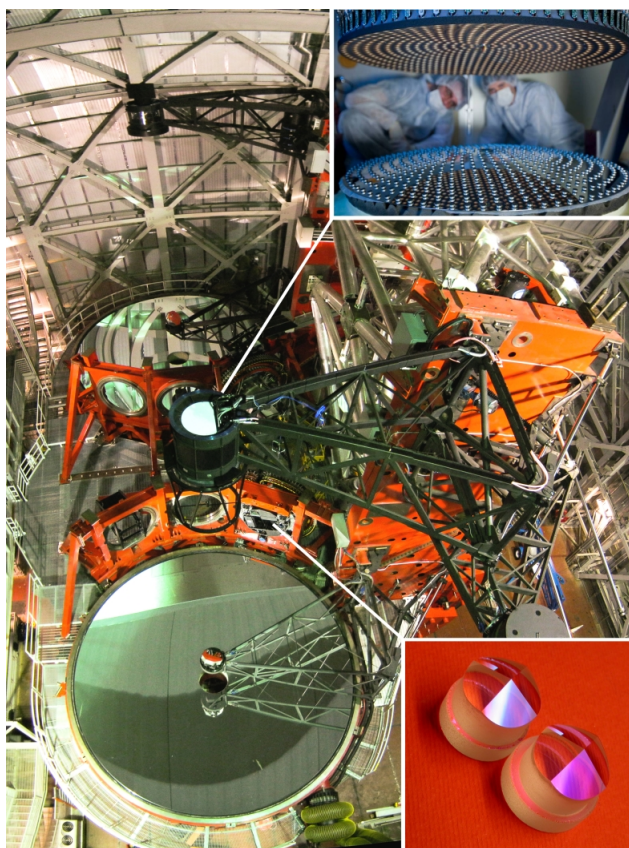
Figure 1. FLAO#1 system installed on the right-side of the Large Binocular Telescope. The Acquisition, Guiding and Wavefront sensing (AGW) unit containing the pyramid WFS is located on the front-right bent-Gregorian focal station. In this photograph the ASM unit features the retro-reflector optics used for system calibrations mounted below it.

2. FLAO SYSTEM OVERVIEW

We will briefly review in this section the general characteristics of the FLAO#1 system as it was commissioned to the telescope (Figure 1). A detailed description of the system optical design and laboratory characterization can be found in the cited papers[2][3].

The ASM is equipped with a Zerodur thin shell of 1.6 mm thickness and 911 mm diameter. It relies on 672 contactless voice-coil force actuators to shape the thin shell with a maximum stroke of ~100μm. The settling time ranges from 0.7 to 1ms, and the best figuring error obtained at the telescope is ~28 nm RMS in wavefront, using approximately the 25% of the forces range[5]. The FLAO#1 commissioning results have been obtained with a total of 641 actuators. The contactless technology allows to software deactivate the 31 defective actuators without introducing hard points on the shell.

The pyramid WFS[6] features a maximum of 30×30 subapertures to sample the mirror shape. The equivalent sampling on the primary mirror is 0.28m which matches the Fried parameter (r_0) obtained under good seeing conditions at the WFS central wavelength of λ_s = 750nm. The WFS camera uses a fast readout E2V CCD39 unit with 80x80 pixels and a maximum frame rate at full frame of f_s =1 kHz.

The temporal and spatial sampling of the WFS can be adjusted as a function of M_R, the equivalent R-magnitude of the guide star (§3.1). In particular, the number of subapertures across the pupil diameter can be easily changed by choosing one of the on-chip CCD binning modes. In this way, the telescope pupil can be sampled with 30×30, 15×15, 10×10, or ~7×7 subapertures when using, respectively, binning modes #1, #2, #3, or #4. The sensitivity of the WFS can also be adjusted by means of the pyramid (circular) modulation.

Table 1. Typical system configurations used on sky as a function of the equivalent R-magnitude of the GS (M_R). The system parameters are: the binning mode, the temporal sampling frequency (f_s), the number of controlled modes (n_{mod}), and the pyramid modulation. Median RON values measured for each configuration are also listed.

M_R	Binning mode	*Pupil sampling (# subaps.)*	f_s (Hz)	n_{mod}	Pyr. mod. ($\pm\lambda_s/D$)	RON ($\sigma_{e\text{-}}$)
$M_R \le 8.0$	1	30×30	990	500	2.0	10.5
$M_R \le 10.0$	1	30×30	990	400	3.0	10.5
$10.0 < M_R < 13.5$	2	15×15	$990 \le f_s \le 300$	153	3.0	6.4
$13.5 \le M_R < 14.5$	3	10×10	$500 \le f_s \le 200$	66	6.0	4.5
$14.5 \le M_R < 16.5$	4	~7×7	$400 \le f_s \le 100$	36	6.0	4.6
$16.5 \le M_R < 18.0$	4	~7×7	100	10	6.0	4.6

The typical system parameters used on sky as a function of M_R are summarized in Table 1. Also in this table are listed the actual Read-Out Noise (RON) median values measured for each system configuration.

The FLAO control system implementation is based on a modal approach. To be more effective in correcting the turbulence, the modal control basis uses Karhunen-Loève (KL) modes fitted by the ASM[7]. The temporal controller is a modal integrator. Since the optimal integrator gains strongly depend on the atmospheric conditions, a procedure to automatically estimate the optimal gains has been developed. This procedure is run just after the Guide Star (GS) is acquired. Currently, gain values are not further changed during normal AO operation.

The modal interaction matrices between the ASM and the WFS (one for each pair of binning mode and pyramid modulation values) were calibrated at the telescope on daytime with the use of the retro-reflector optics[2] installed below the ASM permitting the calibration beam to reach back the WFS unit (Figure 1).

3. OBSERVING CONDITIONS

The maximum performance that can be attained with an AO system is limited by several factors, the most important being the total received flux from the GS, the atmospheric turbulence conditions (i.e. the seeing value, and the wind speed), the separation between the object of interest and the GS, the read-out nosie of the WFS detector, and the telescope vibrations. We will focus in this paper on the on-axis performance results of the FLAO#1 system in terms of the SR in H band as a function of the star magnitude and the atmospheric seeing value. We will describe in this section how we have estimated these two important parameters.

3.1 Equivalent star magnitude in R band

The FLAO's pyramid WFS is sensitive to a broadband encompassing R and I bands. On the lower bound, the passband is limited by a dichroic sending all the light above 600nm to the WFS. On the upper bound, the quantum efficiency curve of the WFS detector ——a deep-depletion CCD39— limits the passband to ~950nm. Therefore, the luminosity of the GS in this band, 600−950nm, drives the AO correction capabilities.

For the purpose of comparing the performance of the FLAO system obtained with different reference stars, we will use the concept of an "equivalent" star magnitude in R band computed as:

$$M_R = -2.5\log_{10}\left[\frac{h \cdot c}{\tau_{sys} \cdot \lambda_s \cdot e_0} n_{ph}\right]$$ (1)

where n_{ph} stands for the number of photons per squared-meter per second [ph m^{-2} s^{-1}]. This quantity can be easily estimated from the acquired WFS CCD39 frames. The constants in Eq. (1) are: h, the Planck constant; c, the light velocity; $e_0 = 1.76 \cdot 10^{-8}$ W m^{-2} µm^{-1}, the zero-magnitude brightness in the Johnson R band; $\lambda_s = 750$nm, the WFS central wavelength; and τ_{sys}, the overall optical transmission (Telescope + WFS board + CCD39) in the spectral band 600−950nm.
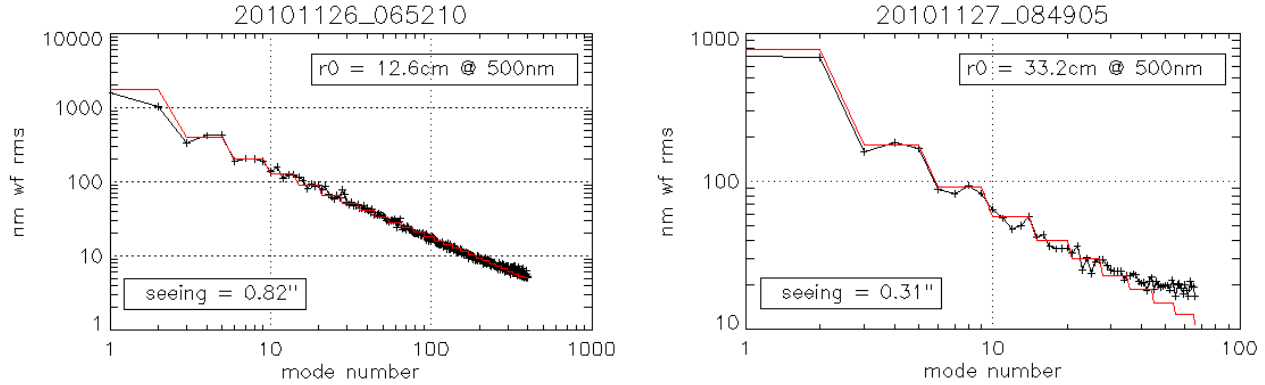
Figure 2. Example of r_0 fitting from reconstructed OL modes. (Crosses) Estimated OL modal variances; (Red line) Theoretical modal variance distribution. (*Left*) Case of bin#1, 400 controlled modes. (*Right*) Case of bin#3, 66 controlled modes.

3.2 Estimation of the seeing value

In order to have an estimate of the turbulence conditions during a given observation, LBT uses a Differential Image Motion Monitor (DIMM) installed on top of the telescope mount, and an anemometer installed on top of the telescope enclosure. An additional estimate of the seeing value can be found using the AO system telemetry data. This on-line seeing estimation method is based on the reconstruction of Open-Loop (OL) modes (i.e. the modal decomposition of the turbulence) from applied ASM commands and residual WFS signals acquired during the closed-loop operation of the AO system[8]. Once the OL modes are available, the Fried parameter (r_0) can be estimated from the OL modal variance distribution, from which the seeing value can be simply computed as $s(\lambda)=0.98\lambda/r_0$ (by convention $s(\lambda)$ quoted at λ=500nm).

Figure 2 shows the seeing estimation results for two particular cases. The plots show the time-variance distribution of the reconstructed OL modes, and the best-fit theoretical (Kolmogorov) variance distribution of Zernike modes. In order to avoid the uncertainty of the outer scale of the turbulence (L_0) and the residual telescope vibrations, the first three radial orders are not considered in the fitting. Nor we have considered the last two radial orders, most likely affected by aliasing. Despite the good fitting achieved in both cases shown in Figure 2, we should note that the seeing estimation for the case of binning #3 and 66 controlled modes is actually under-estimated. Indeed, the mismatch between the PSF size during the calibration of the interaction matrices (diffraction-limited) and the actual PSF size in closed-loop operation at WFS wavelengths is responsible for the underestimation of the modal residuals, which in general leads to an underestimation of the seeing value. We have found from our data analysis that this underestimation is non-negligible for datasets taken with star magnitudes M_R >13. We are currently working on an improvement of the on-line seeing estimation method in which the modal residuals are iteratively estimated.

4. ON-SKY COMMISSIONING RESULTS

We will now present the overall performance analysis of the FLAO#1 system based on the data collected during the commissioning nights. The SR was estimated from the long-exposure PSFs measured with the InfraRed Test Camera[9] (IRTC) using an H-band filter with an effective central wavelength of 1.60μm. Total integration times varied from ~30s for high-flux PSF measurements up to ~120s for the low-flux ones. The camera was operated in the narrow Field-of-View (FoV) mode with a pixel scale of 10 mas/pixel.

Figure 3 summarizes the performance results attained by the FLAO#1 system. A total of 597 Strehl Ratio estimations at star magnitudes from ~7.5 to ~18 are shown in the plot. Seeing values estimated from AO real-time data are coded in color. Points (M_R>13) for which seeing values are strongly under-estimated with this method are shown in black. Figure 3 also indicates which system configuration (i.e. binning mode) has been used for each acquisition. Finally, the expected performance estimated from numerical simulations and for different seeing values (0.6", 0.8", 1.0", 1.2", and 1.5") is also shown in the plot. It is important to note that the measured SR values are in accordance with the simulated ones, showing that the FLAO#1 system meets the expected performance.
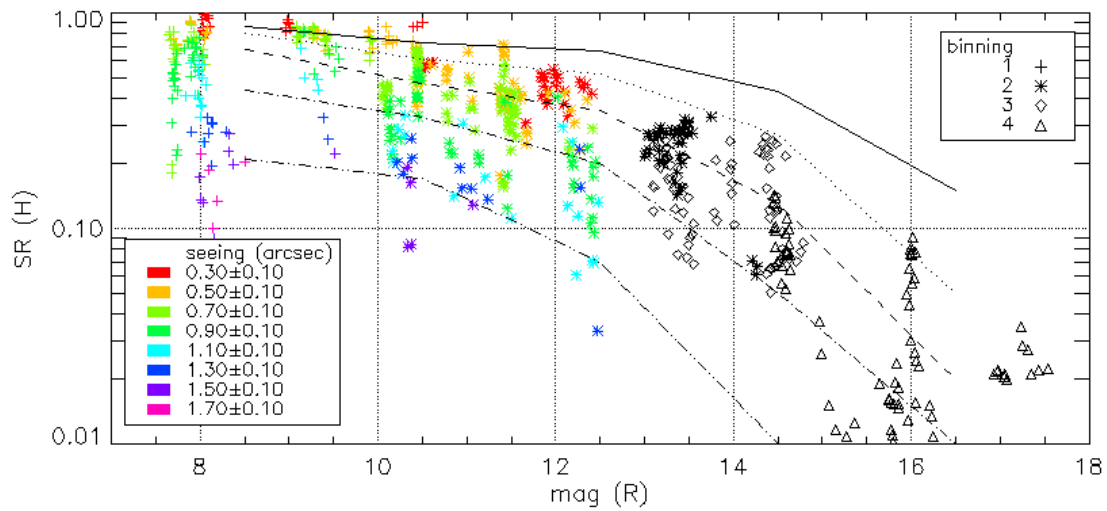
Figure 3. (Color online) Summary plot of FLAO#1 performance commissioning results. Strehl Ratio in H band versus star magnitude (R) and for different seeing values (estimated from AO real-time data). Points (M_R >13) for which seeing values are strongly under-estimated are shown in black. Different binning modes are indicated with symbols. Lines correspond to expected performance from numerical simulations with different seeing values; from top to bottom: 0.6", 0.8", 1.0", 1.2", and 1.5".

Figure 4 shows some examples of AO-corrected PSFs sampling the range of star magnitudes ($8<M_R<17$), and for a seeing value of about 0.8arcsec. Note that a diffraction-limited resolution of 40mas is achieved down to magnitude ~12. In the next subsections we will discuss some particular cases.
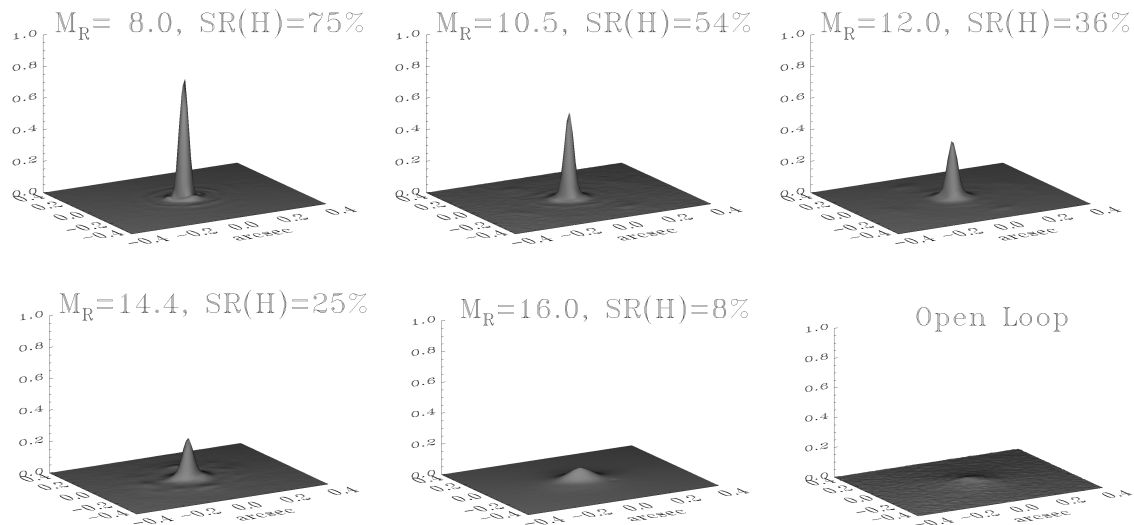
Figure 4. Examples of AO-corrected PSFs (normalized to the diffraction-limited peak) acquired at different star magnitudes. The system configurations are listed in Table 1. The seeing value for all of these acquisitions was about 0.8 arcsec. An OL PSF is also shown for comparison.

4.1 Performance at the bright end: high-contrast imaging

Figure 5 shows an example of a high-order corrected PSF in H band with a SR of >80%. The equivalent R magnitude of the GS (HD175658) is 6.5 and the on-line estimated seeing oscillated between 0.6 and 0.8 arcsec. The AO loop was running at 1 kHz controlling 400 KL modes. Some residual tip/tilt vibrations at ~13.4Hz of 6 to 8 mas rms were present. Figure 5 also shows the radial-averaged profiles of the AO-corrected and the diffraction-limited PSFs. It is important to note that a contrast better than 10^4 is achieved at a radial distance of 0.4 arcsec radius from the central peak, just before the turbulence residual halo occurring at ~0.47 arcsec. This image confirms on sky for the first time the deep annular region where the non-aliased correction offered by the pyramid sensor achieves the maximum contrast[10].
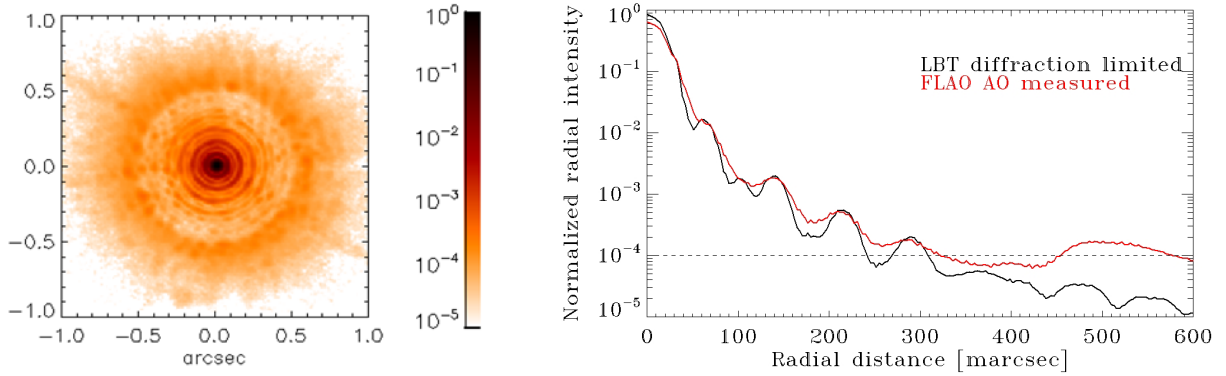
Figure 5. (*Left*) High-order AO-corrected PSF using a bright star (M_R = 6.5) under median seeing conditions (seeing~0.7"±0.1"). (*Right*) Comparison between the diffraction-limited PSF (black full curve) and the AO-corrected PSF profiles (red full curve). Profiles are normalized to the diffraction-limited peak.

4.2 Performance at the faint end

Let us now discuss the performance of the FLAO system with faint reference stars, close to the current limiting magnitude. Figure 6 shows an example of the results obtained at M_R= 17.2. The star observed was LP154-66 (M_R=13.20, M_H=10.17), and a neutral density filter was placed on the WFS channel to emulate a 17.2 R-magnitude star. The system was operated with binning mode #4 and controlling only 10 modes giving a SR(H) of ~3.5%. The FWHM of the AO-corrected PSF is reduced a factor of 1.7 with respect to the seeing-limited one, and their peaks ratio equals 2.6.

A seeing estimate for this acquisition was not available from the DIMM. We can nevertheless use the FWHM of the seeing-limited PSF and, assuming a given outer scale value, estimate the seeing as in Tokovinin(2002)[11]. Following this method, and considering an outer scale of L_0= 40m, we get a seeing estimate of 0.72" (@ 500nm) for this observation.
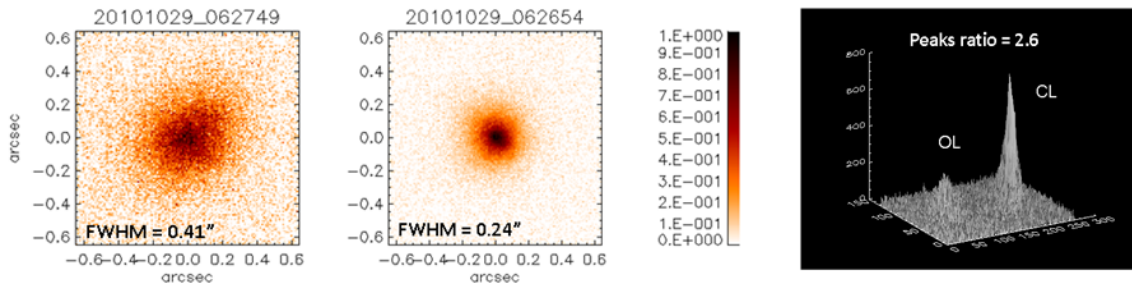
Figure 6. Example of the FLAO performance in H band at its faint end (M_R= 17.2). (*Left*) Seeing-limited image. (*Middle*) AO-corrected image. System parameters: binning mode #4, 10 controlled modes, 100Hz, and a modulation of ±6λ_s/D. Both images are normalized to their peak intensities. (*Right*) Images placed side by side to show the gain in energy concentration. These images were produced from 5 IRTC frames of 3s exposure time each.

5.   NGS AND LGS ADAPTIVE OPTICS SYSTEMS AFTER LBT RESULTS

We discuss in this section the case of adaptive correction on a small FoV, more precisely the FoV limited by the size of the isoplanatic patch of the atmosphere. Recall that the development of Laser Guide Star (LGS) systems to create suitable reference stars for adaptive optics was mostly driven by the relative inefficiency of the first NGS-based AO systems for science applications. Indeed, the efficiency in exploiting the star flux was in the past lower, with the consequence of achieving a limited sky coverage of the order of one to a few percent, in most cases. Also, the fast read-out CCDs were noisier and the efficiency at low flux levels of the wave-front sensors had to be improved.

In the case of the LBT, the quest for efficiency led to the development of its two AO key components. On one hand, the ASM allows to minimize the number of reflections giving the WFS the possibility to catch the light after only three reflections (primary mirror, ASM, and the folding tertiary); on the other hand, the modulated pyramid allows for a gain of the order of 1-2 limiting magnitudes with respect to commonly used Shack-Hartmann sensors[12][13]. In terms of system efficiency, a future upgrade consists in replacing the current WFS camera (E2V CCD 39) with a Low Light Level CCD (LLLCCD) also called Electron Multiplied CCD (EMCCD) as proposed by Carbillet and Riccardi (2010)[14].

5.1 Improving NGS AO performance and Sky Coverage with an LLLCCD

We have evaluated the performance of an LBT-like system using an LLLCCD with the numerical simulator we developed for FLAO performance verification[7]. The main parameters of the LLLCCCD we simulated are the following: 0.1 e$^-$ RMS noise from Clock Induced Charges (CIC), 0.03 e- RMS of RON at 1kfps. The main atmospheric parameters used in the simulations are: seeing of 0.6 arcsec, outer scale of L_0=40m, and a wind speed of 15m/s.

Results of the simulations in terms of SR in K band (2.2μm) as a function of the GS magnitude are reported in Figure 7 for the FLAO system with a CCD39 and with an LLLCCD. As a comparison, we report on the same plot a typical performance curve for the LGS AO system of the Keck telescope, one of the most successful LGS-based AO systems[15]. Performance curves are reported for a seeing value of 0.6 arcsec (median seeing in Mauna Kea[16]). We recall here briefly that the LGS system needs to use an NGS as the reference for the tip/tilt signal that is not provided by the LGS[17]. However, in this case the NGS is used to measure only the overall tip/tilt and so it can be fainter than the usual reference star for an NGS system. Figure 7 shows that the LGS system has a better limiting magnitude with respect to the FLAO NGS cases. For instance, for a SR of 10% in K band, we obtain 18.4 and 19.0 limiting magnitudes for NGS+LLLCCD and LGS respectively. On the other hand, the NGS+LLLCCD system performance is higher than the LGS system up to magnitude 16.8 reaching a SR higher than 70% up to magnitude 15.2. We note that one of the main limitations of LGS performance in the bright end is focus anisoplanatism error[18].
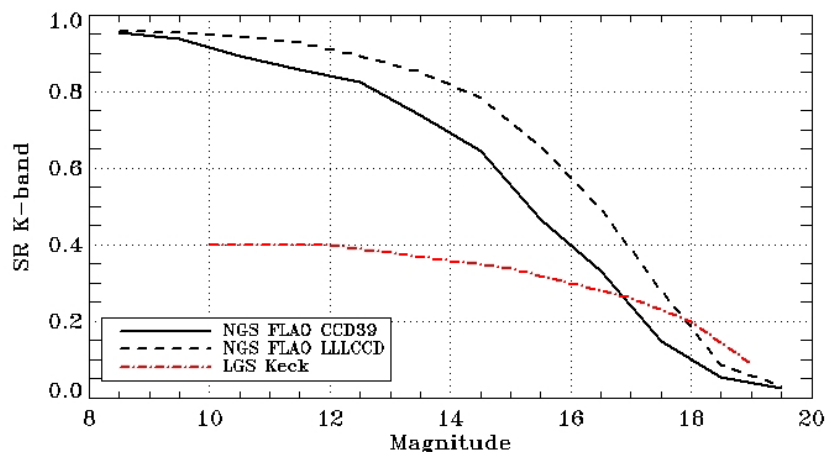

Figure 7. Simulated performance (seeing of 0.6 arcsec) in terms of SR in K band versus star magnitude for the LBT FLAO system and of the improved version using an LLLCCD. The performance of the Keck LGS AO system is shown for comparison.
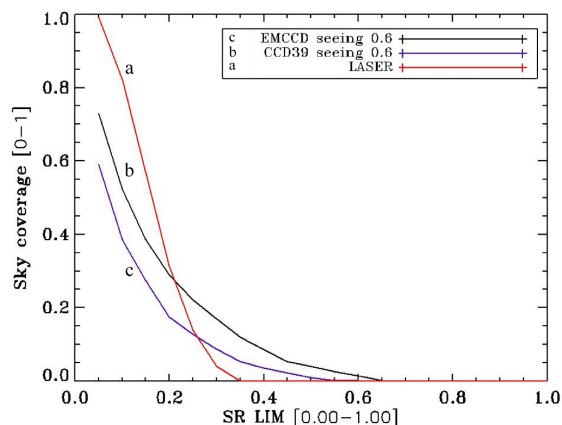
Figure 8 Sky coverage results for the Steidel & al (2003) sample of galaxies using the actual LBT FLAO system (curve c), the improved version using LLLCCD (curve b) and the Keck AO LGS system (curve a). The analyses were made under 0.6"seeing values.

We computed the Sky Coverage (SC) for the two systems in question (NGS+LLLCCD and LGS systems) for a seeing value of 0.6 arcsec with isoplanatic and isokinetic angles of 40 and 73 arcsec respectively in K band. The faint limiting magnitudes considered imply very high sky coverage at low galactic latitudes for both NGS and LGS systems and the comparison is not so interesting. We decided to compute the SC for an astronomical sample of targets located at high galactic latitude. In particular, we selected a sample of about 850 galaxies at z=3 from the Steidel catalog[19] and computed the SR performance according to the plot already shown in Figure 7. The results are shown in Figure 8 where the SC achieved for a given SR is reported for both systems. As a reference, the same curve for the NGS+CCD39 system is also shown in the plot. The result here is that for a required SR of 10% in K band the LGS system achieves an 84% SC while the NGS+LLLCCD system a 54% SC.

On the other hand, for a required SR higher than 25%, the NGS system has a better SC than the LGS system, being on average about 15%. In summary, the above computations show that an LBT-like AO system upgraded from the FLAO system being already demonstrated on sky, has comparable performance to an LGS system as SC is concerned, and has definitely better performance when higher SR values are required.

5.2 Future developments for AO systems

An interesting point about NGS and LGS comparison is the use of adaptive optics systems at wavelengths shorter than the K and H bands like J or even visible wavelengths. Because of the focus anisoplanatism effect, the single LGS correction becomes less and less effective when going to shorter wavelengths[18]. Hence, such a single laser system for an 8m class telescope is limited to correction in K and H band. This limitation does not exist for the NGS system that can be pushed to shorter wavelengths provided a sufficient number of photons and actuators exist. The LBT telescope is a first example of this, having achieved about 50% SR in J band and 20% of SR at 850nm. The scaling of LBT on-sky results to shorter wavelengths is shown in Figure 9. Let us mention that the 6.5 Magellan telescope[20] is in the testing phase of an LBT-like system aimed at visible observations. A similar system could be developed for the ESO UT4 telescope being equipped in the next future with an adaptive secondary having more than 1100 actuators[21]. Such a system could deliver 15 mas FWHM at 0.6 μm. In the LGS case, visible AO requires to solve the focus anisoplanatism issue using more than one LGS and so in turn using more than one NGS for the measurements of wavefront low-order modes[22]. On the other hand, NGS systems do no require major changes to be operational at shorter wavelengths as already discussed.

Finally, if we move to AO systems for ELTs, the design of an LGS system becomes very complex considering the number of LGS and NGS needed, the needs to deal with the spot elongations effect, and several other issues arising from the use of LGS such as the variability of the sodium density profile, etc. On the contrary, an NGS-based system for an ELT is built exactly as a system for an 8m telescope, the only difference being the number of actuators and subapertures. Such considerations summed to the easiness of operation and reduced cost of an NGS-based AO system suggests rethinking the use of LGS in AO to improve system SC and reliability for 8m and ELT class telescopes. This at least for AO systems having the corrected FoV limited by the atmospheric isoplanatic patch.
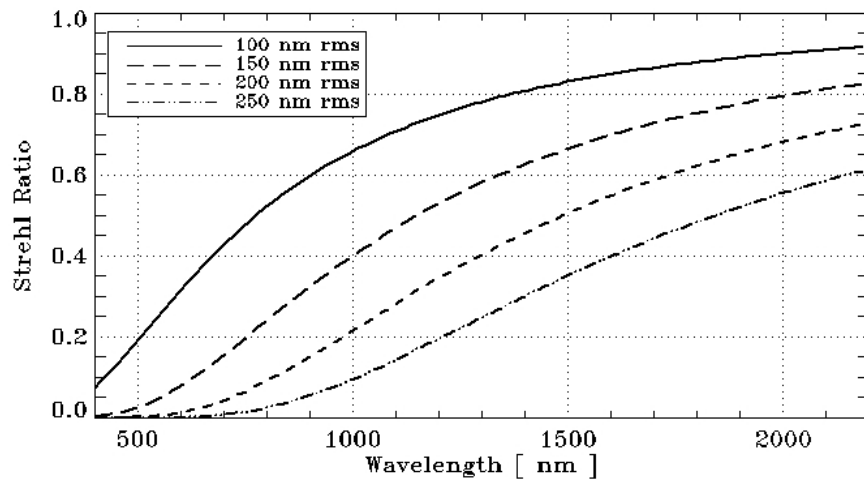
xxx

Figure 9. Strehl Ratio scaling as a function of the wavelength. Each curve represents a different level of wave-front correction corresponding to SR values in H band of 85%, 70%, 55%, and 40%.

6. CONCLUSIONS

The First Light AO system (FLAO#1) of the 2x8.4m LBT telescope has been commissioned on sky in the period from June 2010 to August 2011. The achieved results —such as H band SR higher than 80%, image contrast better than 10^4, and loop closure down to 17.5 magnitude star— sets a new standard for ground based astronomical AO systems. At the same time these results show that adaptive secondary mirrors and pyramid sensors are mature technologies to be used in the design of future AO systems for 8m and ELT class telescopes.

Finally, an elaboration of the LBT experience does show that an LBT-like system using an LLLCCD can achieve, in the case studied of extragalactic objects, a sky coverage of 54% comparable to the one obtained with an LGS of 84%. Moreover, a better sky coverage at SR higher than 25% can be achieved by the NGS system. These results, coupled with relevant limitations of LGS systems like cone effect and the need for low-order modes sensing with an NGS, suggest that the choice of using LGS systems instead of NGS systems to improve AO system efficiency should be revisited.

ACKNOWLEDGEMENTS

REFERENCES

[1] Hill, J. M., "The Large Binocular Telescope," App. Opt. 49(16), D115-D122 (2010).
[2] Esposito, S., Riccardi, A., Quirós-Pacheco, F., Pinna, E., Puglisi, A., Xompero, M., Briguglio, R., Busoni, L., Fini, L., Stefanini, P., Brusa, G., Tozzi, A., Ranfagni, P., Pieralli, F., Guerra, J. C., Arcidiacono, C. and Salinari, P. "Laboratory characterization and performance of the high-order adaptive optics system for the Large Binocular Telescope," App. Opt. 49(31), G174-G189 (2010).
[3] Esposito, S., Riccardi, A., Fini, L., Puglisi, A. T., Pinna, E., Xompero, M., Briguglio, R., Quirós-Pacheco, F., Stefanini, P., Guerra, J. C., Busoni, L., Tozzi, A., Pieralli, F., Agapito, G., Brusa-Zappellini, G., Demers, R., Brynnel, J., Arcidiacono, C., and Salinari, P., "First light AO (FLAO) system for LBT: final integration, acceptance test in Europe, and preliminary on-sky commissioning results," Proc. SPIE 7736, 773609 (2010).

xxxi

[4] Seifert, W., Appenzeller, I., Baumeister, H., Bizenberger, P., Bomans, D., Dettmar, R. J., Grimm, B., Herbst, T., Hofmann, R., Juette, M., Laun, W., Lehmitz, M., Lemke, R., Lenzen, R., Mandel, H., Polsterer, K., Rohloff, R. R., Schuetze, A., Seltmann, A., Thatte, N. A., Weiser, P. and Xu, W., "LUCIFER: a multi-mode NIR instrument for the LBT," Proc. SPIE 4841, 962–973 (2003).

[5] Riccardi, A., Xompero, M., Briguglio, R., Quirós-Pacheco, F., Busoni, L., Fini, L., Puglisi, A., Esposito, S., Arcidiacono, C., Pinna, E., Ranfagni, P., Salinari, P., Brusa, G., Demers, R., Biasi, R., and Gallieni, D., "The adaptive secondary mirror for the Large Binocular Telescope: optical acceptance test and preliminary on-sky commissioning results," Proc. SPIE 7736, 77362C (2010).

[6] Ragazzoni, R., "Pupil plane wavefront sensing with an oscillating prism", J. Mod. Opt. 43(2), 289-293 (1996).

[7] Quirós-Pacheco, F., Busoni, L., Agapito, G., Esposito, S., Pinna, E., Puglisi, A., and Riccardi, A., "First light AO (FLAO) system for LBT: performance analysis and optimization," Proc. SPIE 7736, 77363H (2010).

[8] Fusco, T., Rousset, G., Rabaud, D., Gendron, E., Mouillet, D., Lacombe, F., Zins, G., Madec, P. Y., Lagrange, A. M., Charton, J., Rouan, D., Hubin, N., and Ageorges, N., "NAOS on-line characterization of turbulence parameters and adaptive optics performance," J. Opt. A: Pure Appl. Opt. 6, 585-596 (2004).

[9] Foppiani, I., Hill, J. M., Lombini, M., Bregoli, G., Cosentino, G., Diolaiti, E., Herbst, T. M., Innocenti, G., Meschke, D., Miller, D. L., Rohloff, R. R., and Schreiber, L., "An instrument for commissioning the active and adaptive optics of modern telescopes: the Infrared Test Camera for the Large Binocular Telescope," Exp. Astron. (2011), doi: 10.1007/s10686-011-9229-2

[10] Verinaud, C., "On the nature of the measurements provided by a pyramid wave-front sensor", Opt. Comm. 233, 27-38 (2004).

[11] Tokovinin, A., "From differential image motion to seeing", PASP 114, 1156-1166 (2002).

[12] Ragazzoni, R., Farinato, J., "Sensitivity of a pyramidic wavefront sensor in closed loop adaptive optics", A&A 350, L23-L26 (1999).

[13] Esposito, S., and Riccardi, A., "Pyramid Wavefront Sensor behavior in partial correction Adaptive Optic systems", A&A 369, L9-L12 (2001).

[14] Carbillet, M., and Riccardi, A., "Low-light-level charge-coupled devices for pyramid wavefront sensing on 8 m class telescopes: what actual gain?", App. Opt. 49(31), G167-G173 (2010).

[15] van Dam, M. A., Bouchez, A. H., Le Mignant, D., Johansson, E. M., Wizinowich, P. L., Campbell, R. D., Chin J., Hartman, S., K., Lafon, R. E., Stomski, J. Jr., and Summers, D. M., "The W. M. Keck Observatory Laser Guide Star Adaptive Optics System: Performance Characterization", PASP 118, 310-318 (2006).

[16] Tokovinin, A., Vernin, J., Ziad, A., Chun, M., "Optical Turbulence Profiles at Mauna Kea Measured by MASS and SCIDAR", PASP 117, 395-400 (2005).

[17] Fried, D. L., "Artificial-guide-star tilt-anisoplanatism: its magnitude and (limited) amelioration", OSA Technical Digest Series 23, 363–369 (1995).

[18] Sandler, D. G., Stahl, S., Angel, J. R. P., Lloyd-Hart, M. and McCarthy, D., "Adaptive optics for diffraction-limited infrared imaging with 8-m telescopes", J. Opt. Soc. Am. A 11(2), 925-945 (1994).

[19] Steidel, C. C., Adelberger, K. L., Shapley, A. E., Pettini, M., Dickinson, M. And Giavalisco, M., "Lyman Break Galaxies at Redshift z~3: Survey Description and Full Data Set", Astrophys. J. 592(2), 728-754 (2003).

[20] Close, L. M., Gasho, V., Kopon, D., Males, J., Follette, K. B. and Brutlag, K., "The Magellan Telescope Adaptive Secondary AO System: a visible and mid-IR AO facility", Proc. SPIE 7736, 773605 (2010).

[21] Arsenault, R., Biasi, R., Gallieni, D., Riccardi, A., Lazzarini, P., Hubin, N., Fedrigo, E., Donaldson, R., Oberti, S., Stroebele, S., Conzelmann, R. and Duchateau, M. "A deformable secondary mirror for the VLT", Proc. SPIE 6272, 62720V (2006).

[22] Tallon, M. and Foy, R., "Adaptive Telescope with Laser Probe - Isoplanatism and Cone Effect", A&A 235(1-2), 549-557 (1990).